Clays and Clay Minerals, Vol. 37, No. 6, 532–541, 1989.

Fe-SMECTITE-GLAUCONITE TRANSITION IN HYDROTHERMAL GREEN CLAYS FROM THE GALAPAGOS SPREADING CENTER

MARTINE BUATIER, JOSE HONNOREZ, AND GABRIELLE EHRET

Centre de Sédimentologie et de Géochimie de la Surface,
CNRS, 1 rue Blessig, 67084 Strasbourg, France

Abstract—X-ray powder diffraction (XRD) and energy-dispersive X-ray analyses (EDX) of individual clay particles from hydrothermal mounds in the Galapagos spreading center (GSC) (Deep Sea Drilling Project, hole 509B) and high-resolution transmission electron microscopy (HRTEM) of the <2-μm size fraction of these sediments were carried out to document the mineralogy, geochemistry, and evolution of their clay horizons. The hydrothermal clay minerals of the GSC mounds were found to be intercalated with pelagic sediments and occurred as irregular interstratified illite/smectite according to X-ray powder diffraction analyses. On the basis of TEM, HRTEM, and EDX data, two types of clays appeared to coexist; these types differed in morphology, potassium content, and mode of stacking sequence. Lath-shaped particles having regular 10-Å spacings were identified as glauconite, and filmy or veil-like particles, having curly edges and variable 10–13-Å spacings were identified as Fe-smectite (nontronite and Fe-montmorillonite). The absence of lattice fringes between Fe-smectite and glauconite crystallites was observed by HRTEM in clay aggregates. This structural discontinuity between Fe-smectite and glauconite layers suggests that a dissolution-recrystallization mechanism was responsible for the textural and chemical transition from the filmy Fe-smectite to the lath-like glauconite.

Key Words—Deep-sea hydrothermal clay, Glauconite, Smectite, Transmission electron microscopy, X-ray powder diffraction.

INTRODUCTION

Hydrothermal mounds of the Galapagos spreading center (GSC) in the Equatorial Pacific are made up of several layers of green clays interbedded with siliceous, foraminiferal, and nanofossil calcareous oozes, which are overlain by Fe-Mn oxyhydroxide crusts. The mounds are located in areas of high heat flow (8 to 10 heat flow units) above small, vertical basement faults (Williams *et al.* 1974). Clay minerals in the Galapagos mounds were described by Hoffert *et al.* (1980), Honnorez *et al.* (1981, 1983), Kurnosov *et al.* (1983), and Varentsov *et al.* (1983) as Fe-rich smectite and Fe-rich mica, i.e., nontronite and celadonite, respectively. The origin and subsequent precipitation of these minerals from solutions exiting from a highly permeable ocean basement in the vent area was ascribed by Honnorrez *et al.* (1983) to low-temperature hydrothermal activity; however, these authors did not address the mechanism of formation and evolution of these clays. The present paper characterizes the mineralogy and chemistry of the two types of clay minerals present in the Galapagos hydrothermal mounds and on the basis of observed relationships proposes a possible mechanism for their formation.

GEOLOGICAL SETTING AND SAMPLE SELECTION

Hole 509B, drilled during Deep Sea Drilling Project (DSDP) leg 70, coincides with IPOD-DSDP leg 54, site 424, and is located near 1°N latitude and 86°W longitude on the south flank of the GSC about 22 km from the spreading axis (Figure 1). The drill penetrated 33.4 m of sediment before encountering basement, which was not drilled. Two main lithological units can be distinguished in the hole: an upper unit of green clay interbedded with pelagic oozes (3 to 16 m beneath the sediment-water interface at the top of the mound) and a lower unit of pelagic oozes (16 to 33.4 m). Mn oxide fragments occur in the uppermost 4.3 m of the section (Figure 1). Calcite is the predominant mineral in the pelagic oozes, whereas Mn oxide crusts, which cap the sequence, consist chiefly of todorokite. Chemical analyses of the GSC sediment pore waters suggest that hydrothermal solutions enriched in Ca and depleted in Mg were upwelling through the pelagic oozes and precipitated the green clays (Bender, 1983).

The basement at site 509B is about 0.6 to 0.63 My old, based on a half-spreading rate of 3.5 cm/yr (Klitgort and Mudie, 1974). The age of the green clays is much younger and ranges from 90,000 to 300,000 yr based on uranium isotope dating. Ages for the Mn oxide crusts that overlie these clays are even younger and cluster between 20,000 to 60,000 yr old (Lalou *et al.*, 1983).

Hydrothermal processes in the area of the GSC mounds were indicated by geothermal measurements made at 10-m (±1 m) intervals in the 30-m thick sediments of each hole of DSDP leg 70. These measure-

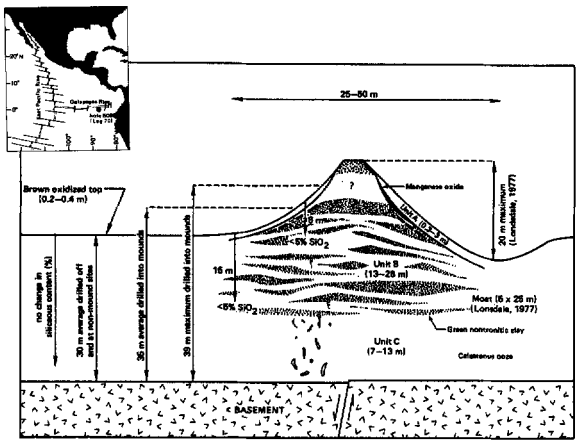

Figure 1. Location of site 509B (Deep Sea Drilling Project leg 70) and schematic diagram of the internal structure and geometry of a hydrothermal mound of the Galapagos Spreading Center (after Honnorez *et al.*, 1983).

ments indicated high and variable total heat flow, with local fluid discharges of about 30°C at $\leq 10^{-8}$ m/s (Becker *et al.*, 1983). A 30-m long core taken near the top of a mound at site 509B with a hydraulic piston corer allowed clay samples to be analyzed from various depths in the same sediment column. Only the green clays from hole 509B were examined in the present study (Figure 2).

EXPERIMENTAL

Preparation techniques

Bulk samples were disaggregated and suspended in water, and the <2-μm clay fraction was separated by standard sedimentation techniques. Chemical treatments were not used to avoid alteration of the clay particles. The <2-μm bulk clay fraction was characterized by X-ray powder diffraction (XRD), wet chemical analysis, and high-resolution transmission electron microscopy (HRTEM). The clay fraction was separated further by means at a Sharples continuous-flux ultracentrifuge into the following size fractions: <0.2 μm, 0.2–0.5 μm, and 0.5–2 μm. The clay particles of the various size fractions were then characterized by XRD and TEM. Elemental analyses of selected clay particles were made for each size fraction.

TEM observations required two different types of preparations. In the first method, clay suspensions were settled onto carbon-coated grids for particle analysis. In the second, ultra-thin sections for stacking-sequence studies by HRTEM were prepared. Clay fractions were impregnated with Spurr resin using the procedure described by Tessier (1984), and after the resin hardened, 500-Å-thick thin sections were obtained using an ultramicrotome (Ehret *et al.*, 1986).

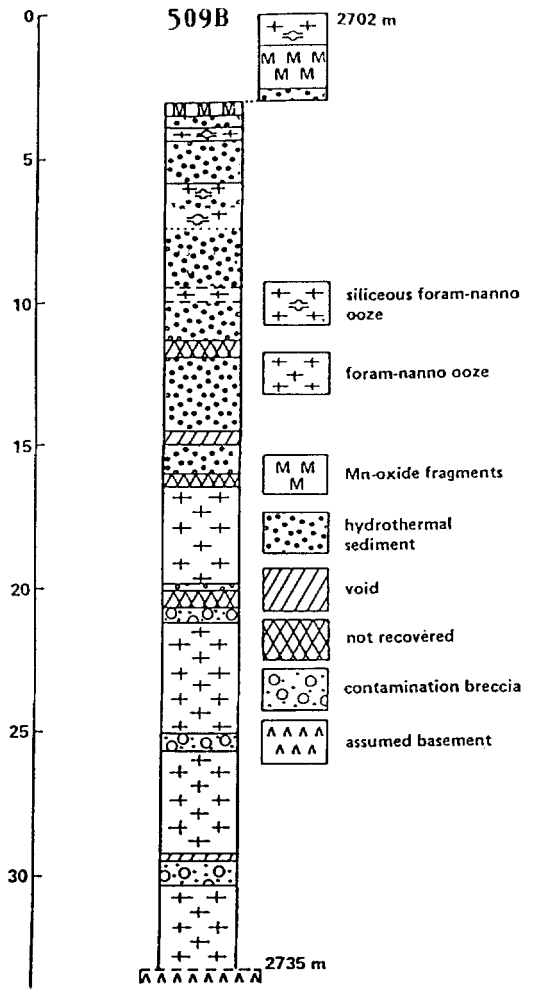

Figure 2. Lithostratigraphy of Deep Sea Drilling Project hole 509B (after Honnorez *et al.*, 1983).

Analytical methods

XRD analyses were made of randomly oriented powders of bulk sediments and of oriented, smear slides of three different clay-size fractions. These samples were air dried, glycolated, and heated for 4 hr at 490°C. XRD analyses were performed using Ni-filtered CuK_α radiation at 40 kV and 18 mA, using 0.1–1.0° slits and a 1°2θ/min scanning speed. Major element analyses of bulk samples were made following the method described by Samuel *et al.* (1985) using arc spectrometry and an ARL quantometer. TEM (bright field images and electron diffraction patterns) and HRTEM studies were carried out with a Philips EM 300 instrument operated at 100 kV. Elemental analyses of single clay particles were made using a TEM-STEM Philips EM 400 equipped with a Tracor SN 2000 energy-dispersive X-ray (EDX) detector, operated at 80 kV, with a 100-Å beam. The elemental abundances were calculated from

https://doi.org/10.1346/CCMN.1989.0370605 Published online by Cambridge University Press

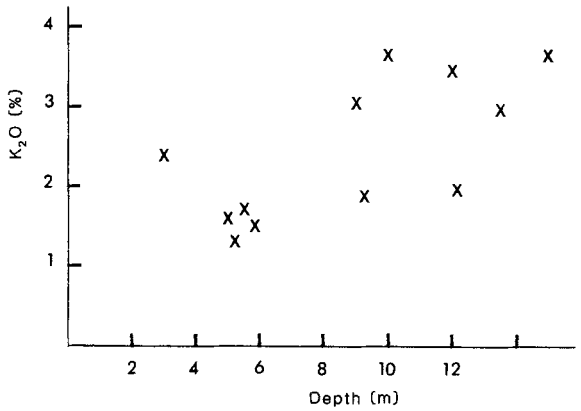

Figure 3. Depth vs. K_2O content of bulk clay-fraction sample as determined by wet chemical analyses.

peak areas applying the Castaing relationship (Tixier, 1978; Paquet *et al.,* 1987), with reference to a phlogopite standard, and the structural formulae of 64 clay particles were calculated. Octahedral and tetrahedral compositions were calculated assuming total structural iron to be present as Fe^{3+}, because the EDX analyses were unable to distinguish Fe^{2+} from Fe^{3+}. This assumption, however, is reasonable because wet chemical analyses carried out on the <2-μm size fractions showed very little or no Fe^{2+} (Honnorez *et al.,* 1983).

RESULTS

Wet chemical analyses

Chemical analyses of the bulk clay samples in Table 1 show that Si and Fe were the predominant elements. Figure 3 shows that the K_2O content of the clay fraction increased with depth in the core.

XRD data

Bulk clay samples. XRD analyses of the randomly oriented powders of the bulk sediment indicate that the GSC green clays coexisted with accessory components, such as halite, calcite, and iron oxyhydroxide. Mn oxyhydroxide (todorokite) was also identified in samples 509B 1-2, 140–150 and 509B 2-2, 70–77. The 060 peak of the phyllosilicate component of these samples was recorded at 1.51 Å (Figure 4), clearly indicating the predominantly dioctahedral nature of the phyllosilicate constituents.

XRD patterns from oriented, smear slides of the <2-μm bulk clay fraction displayed asymmetric 001 reflections. The 001 reflection of the air-dried clay fraction was broad and ranged from 11.5 to 16 Å. It expanded to 17 Å on glycolation and collapsed to 9.8–10 Å on heating. These observations indicate that the <2-μm bulk clay fraction consisted essentially of irregular illite/smectite (I/S), i.e., non-expandable/expandable layers, irregularly interstratified. The percentages of illite layers in the I/S were estimated using modeling methods of Mossman (1987) and Rinckenbach (1988) from the Hendricks and Teller (1942) interstratification formula. Calculated illite contents ranged from 30% in shallow samples to 65% in samples from the deepest part of the drill core (Figure 5).

<0.2-, 0.2–0.5-, 0.5–2-μm size fractions. In most samples the percentage of illite layers in the I/S of the three different grain-size fractions increased with decreasing grain size. In the <0.2-μm size fraction, the percentage of illite layers also increased from the top of the mound to the bottom. This change in illite content can be seen in Figures 6a and 6b from the assymetry of the I/S 001 peak, which becomes steadily more asymmetric as the percentage of illite layers increases.

TEM data

Bulk clay samples. TEM of bulk clay samples showed three types of particles: (1) Filmy or veil-like particles, 1–2 μm in diameter, that had curly edges; these particles were noted as thick as 0.5 μm (Figure 7a); (2) laths as long as 0.5 μm, which were thinner than the

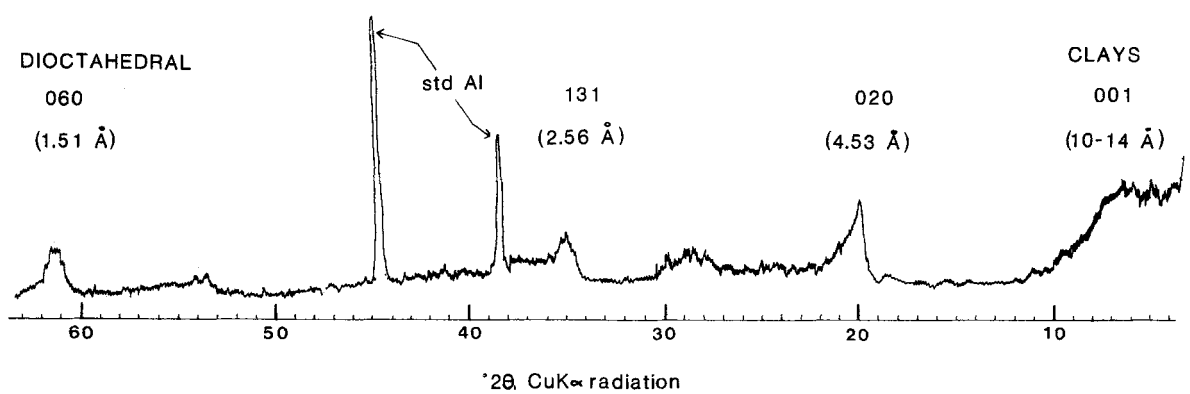

Figure 4. X-ray powder diffraction pattern of randomly oriented clay powders (Deep Sea Drilling Project hole 509B, sample 509B 4-1, 47–50) showing the characteristic peaks of the clay minerals present.

https://doi.org/10.1346/CCMN.1989.0370605 Published online by Cambridge University Press

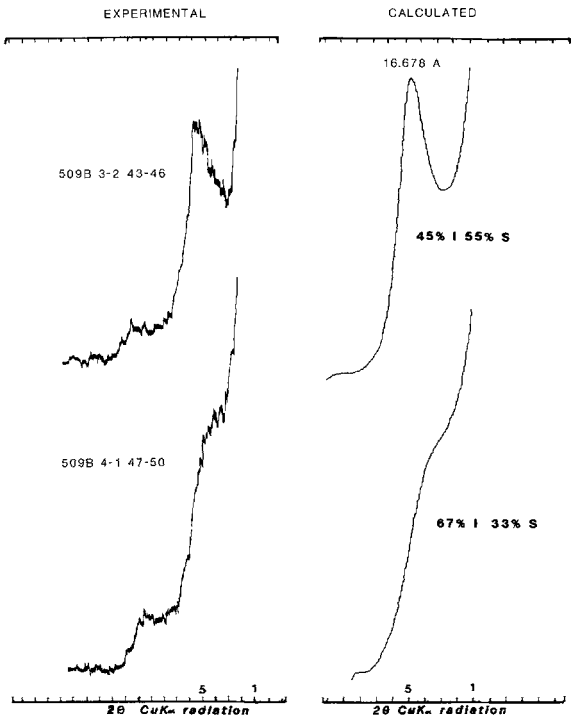

Figure 5. Comparisons of calculated and observed X-ray powder diffraction patterns of oriented smear slides of <2-μm bulk clay fractions. Patterns are similar to that of illite/smectite having 45% illite layers in sample 509B 3-2, 43–46 and 67% illite layers in sample 509B 4-1, 47–50.

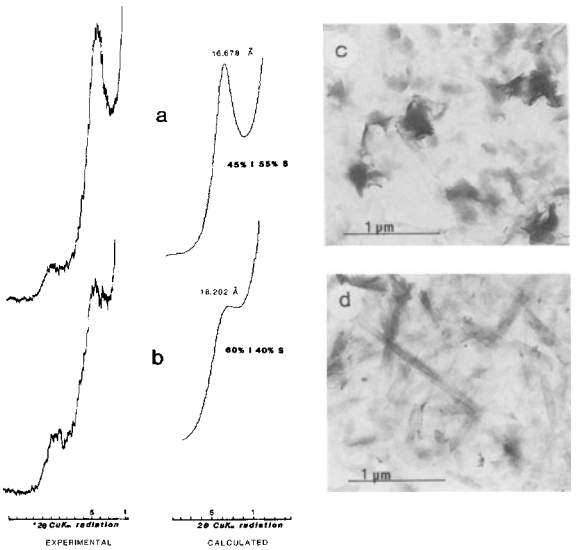

Figure 6. Transmission electron micrographs showing (c, d) particle morphologies in the <0.2-μm bulk clay fractions from various depths in DSDP hole 509B and (a,b) their respective X-ray powder diffraction pattern. Figures 6a and 6c = sample 509B 1-2, 140–150. Figures 6b and 6d = sample 509B 4-1, 47–50.

filmy, veil-like particles (Figures 7e and 7f); and (3) particles having a morphology intermediate between those described as laths and veils (Figures 7c and 7d). The intermediate particles displayed lath-like shapes protruding from the edges of filmy, veil-like particles (Figures 7b, 7c, and 7d). Similar clay mineral assemblages were described by Holtzapffel *et al.* (1985) from North Atlantic Cretaceous-Paleocene sediments.

<0.2-, 0.2–0.5-, 0.5–2-μm size fractions. The separation of the bulk clay into three different particle-size fractions succeeded in isolating the three different particle types. Filmy, veil-like particles and intermediate particles dominated the coarser size fractions, whereas laths tended to concentrate in the finest fraction (<0.2 μm). In the <0.2-μm size fraction, however, morphological differences between samples were observed by TEM. As shown in Figure 6c and 6d, laths were uncommon in the shallowest samples (N°509B 1-2, 140–150, N°509B 2-2, 14–17, N°509B 2-2, 70–77) and were abundant in the deepest samples. In samples 509B 4-1, 47–50 and 509B 4-3, 40–47, taken from the deepest part of the 30-m-long core, the laths showed the highest degree of crystallinity according to their strong electron diffraction pattern.

EDX analyses of single particles

Elemental analyses of single clay particles by EDX varied widely among particle types; hence, only general trends can be inferred (Table 2). No significant variation in total Fe between the different particle types, was observed. Potassium was the most variable element (Figure 8), with the most potassium being present in lath-like particles and lesser amounts in the filmy, veil-like particles. The octahedral compositions are plotted in Figure 9 along with the conventional limits of dioctahedral and trioctahedral smectite (Weaver and Pollard, 1973; Foster, 1960). According to Weaver and Pollard (1973) and Foster (1960), the total number of trivalent cations in the octahedral site must exceed 1.3 per half-unit cell for a dioctahedral smectite, whereas the number of divalent cations must exceed 1.83 per half-unit cell for a trioctahedral phase. As can be seen in Figure 9, all of the clay particles examined from the GSC hydrothermal mounds were dioctahedral. Octahedral, tetrahedral, and layer charges were calculated for each analysis and plotted on a charge diagram (Figure 10), along with the glauconite and smectite domains, as designated by Koster (1982) and Weaver and Pollard (1973). As shown in Figure 10, typical glauconite, a 10-Å dioctahedral mica, is characterized by a low tetrahedral charge and a high interlayer potassium content, whereas Fe-smectite has a lower potassium content and layer charge. As suggested from this illustration, the lath-like particles from the clays of the GSC hydrothermal mounds have both glauconitic and

https://doi.org/10.1346/CCMN.1989.0370605 Published online by Cambridge University Press

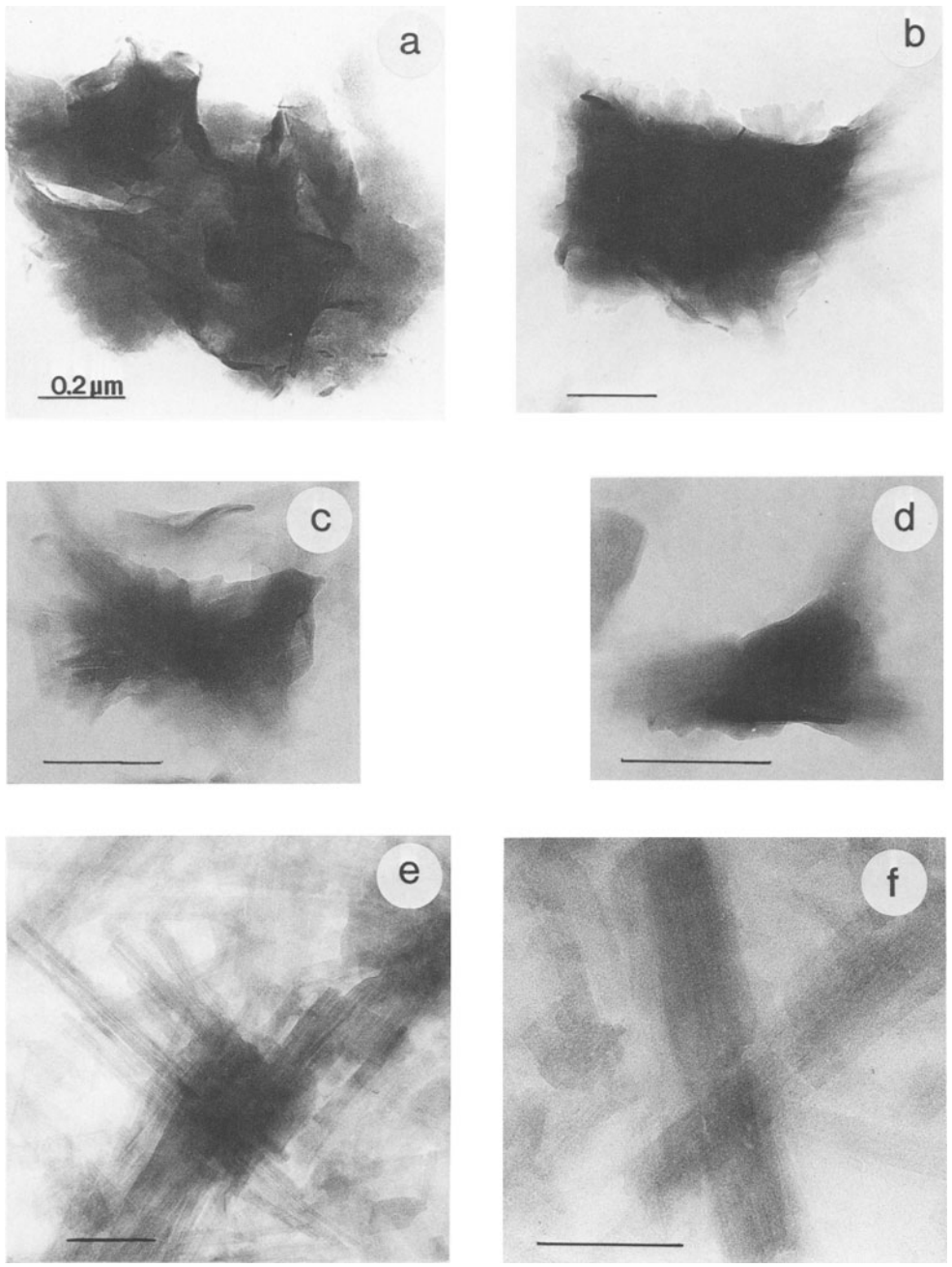

Figure 7. Transmission electron micrographs showing various clay morphologies. (a) Filmy, veil-like particles having curled edges; (b, c, d) "intermediate" particles; (e, f) lath-like particles.

Fe-smectitic compositions, whereas most of the filmy, veil-like particles, have a Fe-smectite composition, i.e., Fe-montmorillonite or nontronite. Five particles had apparently no layer charge. Particles having morphologies intermediate between the lath-like particles and the filmy, veil-like particles plotted in both the glauconite and the Fe-smectite domains. Thus, two major groups of clay mineral were distinguished by the EDX analyses: glauconite and Fe-smectite. These two mineral types also showed distinct textural differences, the glauconite generally displaying lath-shaped morphologies and most of the Fe-smectite particles having veil-like morphologies.

HRTEM data

Particle stacking sequences were studied by HRTEM of ~500-Å thick, ultramicrotome thin sections. The particles were generally composed of several crystal-

https://doi.org/10.1346/CCMN.1989.0370605 Published online by Cambridge University Press

Table 1. Chemical composition of bulk clay fractions of green layers from the Galapagos Spreading Center mounds (Deep Sea Drilling Project, leg 70, hole 509B).

Sample: Depth (cm):	509B 1-2 (143–144)	509B 2-2 (14–17)	509B 2-2 (73–74)	509B 3-2 (42–43)	509B 3-2 (120–121)	509B 3-3 (42–43)	509B 4-4 (42–43)	509B 4-1 (48–49)	509B 4-2 (42–43)	509B 4-3 (42–43)
SiO_2	51.7	52.6	51.9	54.2	53.9	53.7	52.1	50.1	53.6	53.2
Al_2O_3	0.2	0.2	6.5	0.2	8.1	0.2	0.6	9.8	0.3	0.2
MgO	3.072	3.51	4.41	3.37	4.68	3.62	3.49	4.61	3.68	3.95
CaO	0.3	0.6	0.7	0.2	0.5	0.2	0.2	0.6	0.2	0.2
Fe_2O_3	34.5	32.5	22.2	32.1	19.4	30.7	31.5	15.6	30.7	30.6
Mn_3O_4	0.187	0.655	0.355	0.088	0.226	0.065	0.064	0.229	0.076	0.071
TiO_2	0.03	0.06	0.25	0.06	0.31	0.05	0.08	0.41	0.04	0.04
BaO	0.01	0.03	0.37	0.03	0.34	0.06	0.07	0.47	0.03	0.01
P_2O_5	0.1	0.1	0.14	0.1	0.13	0.1	0.1	0.14	0.1	0.1
SrO	0.01	0.01	0.02	0.01	0.03	0.01	0.01	0.04	0.01	0.01
Na_2O	0.79	1.04	0.76	0.96	0.72	0.81	0.81	0.49	0.67	0.47
K_2O	2.43	1.63	1.74	3.08	1.83	3.71	3.43	1.99	2.99	3.68
LOI	6.73	7.32	10.54	5.92	9.6	6.76	7.89	14.88	8.88	8.03
Total	100.34	100.25	99.99	99.91	99.75	99.92	100.14	99.36	101.13	100.12

Major elements are given as oxide weight percentage. LOI = loss on ignition.

lites, which are defined here as single crystals limited by grain boundaries. Glauconite-like layers were rigid, straight, and dislocation-free, whereas Fe-smectite-like layers were generally curled and commonly displayed linear defects, such as edge dislocations (Figures 11a and 11b). Glauconite crystallites commonly had spindle shapes and generated strong electron diffraction patterns, the 001 reflections of which indicated a well-

Table 2. Typical structural formulae on basis of $(O_{10}(OH)_2)$ of the single clay particles based on the energy dispersive X-ray analyses.

Filmy, veil-like particles							
Si	3.97	3.90	3.89	3.80	3.89	3.94	3.86
Al IV	0.03	0.00	0.00	0.18	0.00	0.06	0.14
Fe IV	0.00	0.09	0.11	0.02	0.11	0.00	0.00
Al VI	0.04	0.00	0.00	0.00	0.00	0.84	0.20
Fe VI	1.41	1.50	1.21	1.64	1.57	0.79	1.29
Mg	0.66	0.56	1.06	0.56	0.55	0.59	0.71
K	0.35	0.48	0.33	0.1	0.29	0.02	0.21
O.C.	0.33	0.37	0.25	+0.06	0.19	+0.07	0.11
T.C.	0.03	0.10	0.11	0.20	0.11	0.06	0.14
I.C.	0.36	0.47	0.36	0.14	0.30	0.01	0.25
Intermediate particles							
Si	3.94	3.93	3.89	3.75	3.82	3.92	3.74
Al IV	0.00	0.00	0.11	0.00	0.12	0.08	0.00
Fe IV	0.06	0.07	0.00	0.25	0.06	0.00	0.26
Al VI	0.00	0.00	1.43	0.00	0.00	0.29	0.00
Fe VI	1.41	1.53	0.70	1.43	0.39	1.31	1.33
Mg	0.77	0.00	0.00	0.79	0.91	0.50	0.81
K	0.29	0.40	0.42	0.36	0.18	0.25	0.56
O.C.	0.23	0.41	0.31	0.13	0.01	0.20	0.37
T.C.	0.06	0.07	0.11	0.25	0.18	0.08	0.26
I.C.	0.29	0.48	0.42	0.38	0.19	0.28	0.56
Lath-like particles							
Si	3.93	3.77	3.92	3.62	3.87	3.82	3.68
Al IV	0.00	0.00	0.08	0.17	0.01	0.00	0.07
Fe IV	0.08	0.23	0.00	0.21	0.12	0.18	0.24
Al VI	0.00	0.00	0.05	0.00	0.00	0.00	0.00
Fe VI	1.46	1.25	1.39	1.17	1.36	1.41	1.47
Mg	0.51	0.96	0.62	0.97	0.72	0.66	0.63
K	0.64	0.57	0.49	0.91	0.50	0.60	0.65
O.C.	0.60	0.33	0.44	0.55	0.42	0.45	0.45
T.C.	0.04	0.23	0.08	0.38	0.13	0.18	0.22
I.C.	0.64	0.56	0.52	0.93	0.55	0.63	0.67

O.C. = octahedral charges; T.C. = tetrahedral charges; I.C. = interlayer charges.

https://doi.org/10.1346/CCMN.1989.0370605 Published online by Cambridge University Press

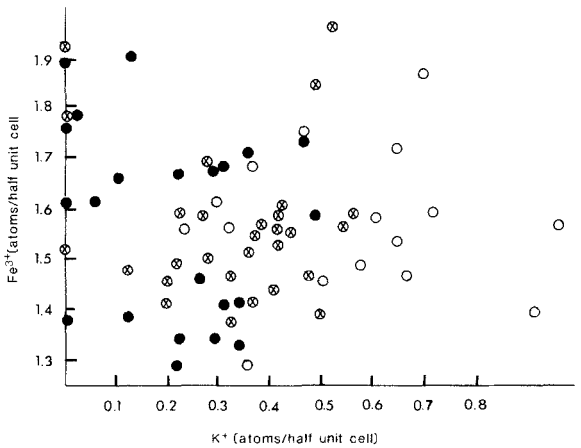

Figure 8. Octahedral compositions of individual clay particles: ● = veil-like particles; ⊗ = intermediate particles; ○ = lath-like particles.

organized structure. On the other hand, Fe-smectite crystallites displayed electron diffraction patterns having weak and diffuse 001 reflections, indicating that they were more poorly crystalline. In the section examined, the glauconite crystallites possessed a 10-Å, regular stacking sequence (Figure 11a) in which six or seven layers made up a single crystallite, unlike the Fe-smectite crystallites which showed 10–13-Å irregular stacking sequences, generally consisting of >10 layers (Figure 12).

Some glauconite crystallites appeared to be sandwiched together with Fe-smectite (Figure 12a) forming a complex, irregularly "interstratified" stacking sequence. This structure probably corresponds to the "intermediate" particles observed by TEM. The glauconite crystallites commonly displayed a stacking sequence parallel to the smectite layers, but no lateral continuity between the smectite and mica-type layers was noted (Figure 12b). These structural discontinuities between the glauconitic and smectitic layers were marked by the absence of lattice fringes and suggest a noncrystalline material (Amouric and Parron, 1985).

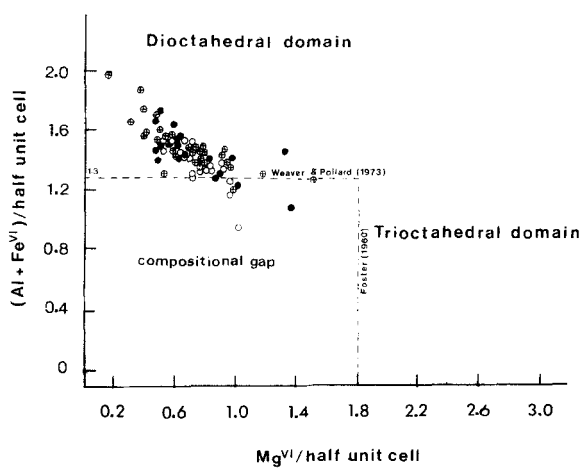

Figure 9. Fe^{3+}/K^+ diagram of clay particles having different morphologies. ● = filmy, veil-like particles, ⊕ = intermediate particles, ○ = lath-like particles.

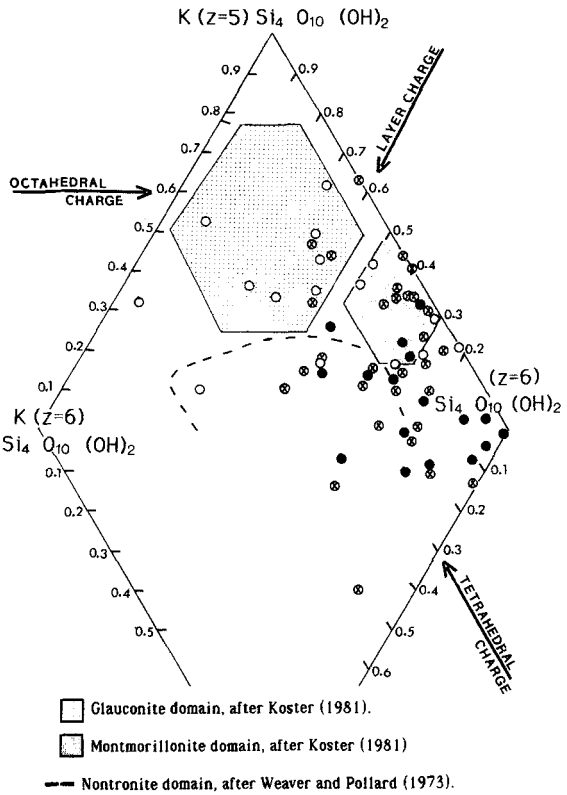

Figure 10. Charge distribution (on the basis of 22 negative charges) in structural formulae of clay particles.

DISCUSSION

Fe-smectite and glauconite

The EDX, XRD, and TEM analyses suggest two types of clay minerals in the hydrothermal mounds of the Galapagos Spreading Center. On the basis of XRD of the <2-μm bulk clay fraction, these dioctahedral, Fe-rich clays are irregularly interstratified I/S, supporting the earlier reports of Hoffert *et al.* (1980), Honnorez *et al.* (1983), and Kurnosov *et al.* (1983) for clays at other sites on the flank of the GSC. These two clay minerals were characterized by Honnorez *et al.* (1983) by means of bulk chemical analyses, TEM, and XRD as "irregular mixed-layer nontronite/celadonite." EDX and HRTEM analyses of the present study have provided more reliable chemical and structural compositions for the various types of clay particles and suggest that the clays are actually Fe-smectite (nontronite and Fe-montmorillonite) and glauconite.

https://doi.org/10.1346/CCMN.1989.0370605 Published online by Cambridge University Press

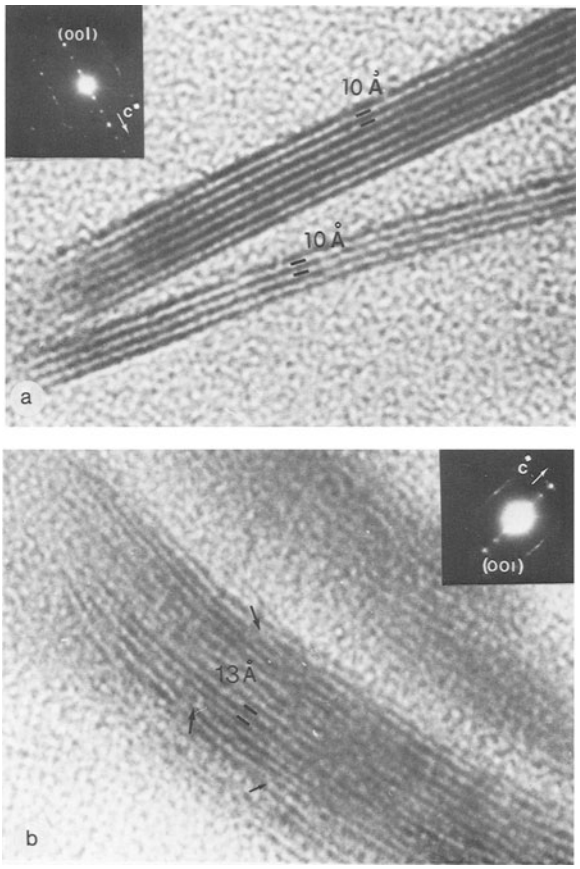

Figure 11. High-resolution electron micrographs showing (a) glauconite crystallite having regular and defect-free stacking sequence and (b) Fe-smectite crystallite having layer widths of 10–13 Å and edge dislocations, as indicated by arrows.

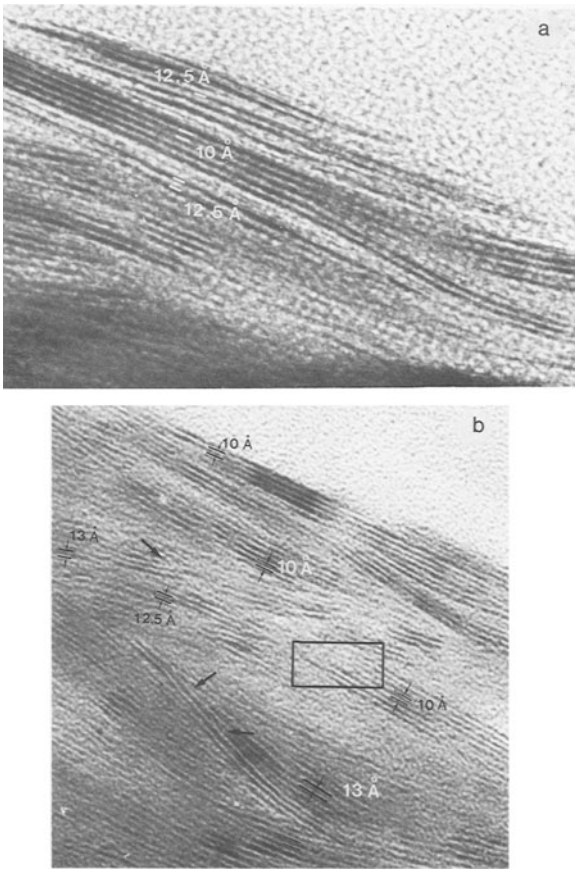

Figure 12. High-resolution electron micrographs showing (a) aggregates of Fe-smectite and glauconite crystallites; glauconite layers are subparallel to Fe-smectite layers. (b) Spindle-shaped glauconite crystallites are in a Fe-smectite matrix containing many edge dislocations (arrows); note discontinuity between the two minerals shown in the rectangle.

Although celadonite and glauconite are both green clays that form in marine environments, celadonite has been considered to be hydrothermal in origin, whereas glauconite has generally been thought to form in shallow sedimentary basins (see, e.g., Foster, 1969). Because the wet chemical analyses of the bulk clay fraction reported by Honnorez *et al.* (1983) did not distinguish between smectite and "illite-type" particles, the "illite" phase in the green clays from the GSC was considered to be a celadonite because of its hydrothermal origin (Honnorez *et al.,* 1983; Kurnosov *et al.,* 1983). On the basis of EDX data, most lath-like particles examined in the present study, fell in the glauconite domain designated by Koster (1982) and Bailey *et al.* (1984), and most of the filmy, veil-like particles plotted in the range defined for Fe-smectite.

Fe-smectite-glauconite transition mechanism

TEM observations and single-particle EDX analyses suggest that the Fe-smectite particles were replaced by glauconite. The facts that lath-like particles of glauconite were common at the edges of the filmy, veil-like particles of Fe-smectite and that the entire morphological spectrum from veil-like particles to lath-like particles was present (Figures 6b, 6c, and 6d) suggest that a veil-like to lath-like textural transition took place. This transition also appears to have been accompanied by a chemical change, as shown by the increased amount of interlayer K in the glauconite vs. the Fe-smectite.

The mechanism for the glauconitization of smectite was described by Hower (1961) and Thompson and Hower (1975) as being due to an addition of K to smectite interlayers without destruction or change of the smectite structure. On the other hand, Amouric and Parron (1985) proposed a neoformation mechanism, by which smectite dissolves, and glauconite crystallizes in its place.

The question of transformation vs. neoformation has been discussed in many papers with reference to the smectite-to-illite transition (e.g., Lee *et al.,* 1985; Ahn and Peacor, 1986a, 1986b; Yau *et al.,* 1987). Other

https://doi.org/10.1346/CCMN.1989.0370605 Published online by Cambridge University Press

studies, however, have interpreted the occurrence of irregular and regular I/S in clays from the Shizan hydrothermal alteration area of Japan and in Wyoming bentonite to be due to a gradual change of smectite to illite by means of a combination of both transformation and neoformation mechanisms (Inoue *et al.*, 1987; Whitney and Northrop, 1988). In one of these studies, in which TEM was used to observe mineral morphology, Inoue *et al.* (1987) described irregular interstratified I/S having 50–100% expandable layers in the form of flake-shaped particles, whereas regular interstratified I/S containing 0–50% expandable layers occurred as flake and lath-like particles. Inoue *et al.* (1987) also reported that the laths gradually increased in width as the percentage of expandable layers decreased and that the K content did not vary with particle morphology. The smectite-to-illite transition as described by Inoue *et al.* (1987) and Whitney and Northrop (1988) was initiated by the fixation of K by smectite, which resulted in irregular interstratified I/S according to XRD. This stage of alteration was followed by the dissolution of smectite and the crystallization of illite, which appeared as regular interstratified I/S in XRD. Their proposed transition mechanism, however, cannot explain the Fe-smectite and glauconite relationships observed in the present study of the hydrothermal green clays of the GSC. In contrast to observations reported in the above studies, the randomly interstratified I/S in the clays of the GSC mounds occurred as two distinct types of particles, which differed in both morphology (i.e., veil-like vs. lath-like) and K content.

On the basis of the textures and chemical analyses reported in the present study, a mechanism for the smectite-to-glauconite transition can be proposed. The occurrence of discontinuities between Fe-smectite having highly imperfect, discontinuously anastomosing layers and glauconite crystallites having straight and relatively defect-free 10-Å layers suggests a dissolution-precipitation mechanism, as proposed by Amouric and Parron (1985). On the basis of the present HRTEM observations, glauconite appears to have inherited its layer orientation from the Fe-smectite structure, because the glauconite crystallites are subparallel to the smectite matrix, their large grain boundaries being parallel to (001).

XRD data indicate an increase with depth in the proportion of glauconite layers in the irregular interstratified I/S. This increase in the proportion of glauconite layers is supported by chemical analyses of the bulk clay fraction, which show that the K content increased with depth in the core (Figure 3). This downward increase in K content in hole 509B is attributed to the reaction of smectite and upwelling solutions or pore fluids. Thus, the clays in the hydrothermal mounds formed in two stages: (1) the initial formation of smectite was a result of the interaction between low-temperature, hydrothermal solutions and pelagic sediments (Honnorez *et al.*, 1983); and (2) glauconite in the lowest part of the mound formed by the dissolution of smectite and subsequent precipitation. This mineralogical change represents a trend towards more perfect, homogeneous, dislocation-free crystallites. The smectite-to-illite transition described from sedimentary basins is also characterized by the same textural and chemical characteristics, but this has generally been ascribed to increasing temperature and depth in the sediment pile (Lee *et al.*, 1985; Mossman, 1987). In the GSC mounds, the smectite-to-glauconite transition appears to have taken place at shallow depth and at ~40°C (Buatier *et al.*, 1988).

SUMMARY AND CONCLUSIONS

1. Green clays from hydrothermal mounds of the Galapagos Spreading Center consist of two types of dioctahedral, Fe-rich clay minerals, namely, filmy, veil-like particles of Fe-rich smectite (Fe-montmorillonite and nontronite) and lath-like particles of glauconite.

2. From HRTEM, the glauconite appears to consist of a regular, 10-Å, defect-free stacking sequence; whereas, the Fe-smectite consists of variable 10–13-Å stacked layers. The glauconite crystallites are commonly oriented parallel to the smectite matrix structure; however, no direct lateral continuity has been observed between them. On the contrary, discontinuities are visible along strike between glauconite and smectite layers.

3. Fe-smectite and glauconite represent two successive stages in the formation of the green clays in the GSC hydrothermal mounds: (a) initial formation of filmy, veil-like, Fe-smectite as a result of the reaction between circulating hydrothermal solutions and pelagic sediments, and (b) the dissolution of Fe-smectite and the precipitation (neoformation) of lath-like particles of glauconite. The glauconite crystallization appears to have taken place preferentially in the deepest part of the sediment column.

REFERENCES

Ahn, J. H. and Peacor, D. R. (1986a) Transmission and analytical electron microscopy of the smectite-to-illite transition: *Clays & Clay Minerals* **34,** 165–179.

Ahn, J. H. and Peacor, D. R. (1986b) Transmission electron microscope data for rectorite: Implication for the origin and structure of "fundamental particles": *Clays & Clay Minerals* **34,** 180–186.

Amouric, M. and Parron, C. (1985) Structure and growth mechanism of glauconite as seen by high-resolution transmission electron microscopy: *Clays & Clay Minerals* **33,** 473–482.

Bailey, S. W., Brindley, G. W., Fanning, D. S., Kodama, H., and Martin, R. T. (1984) Report of The Clay Minerals Society Nomenclature Committee for 1982 and 1983: *Clays & Clay Minerals* **32,** 239–240.

Becker, K., Von Herzen, R. P., and Karato, S. (1983) Geothermal measurements from drilling of sediments near the Galapagos Spreading Center 86°W, D.S.D.P. leg 70: in *Init. Repts. Deep Sea Drilling Project,* **70,** J. Honnorez, J. Von

Herzen, *et al.*, eds., U.S. Govt. Printing Office, Washington, D.C., 445–458.

Bender, M. L. (1983) Pore water chemistry of the Mounds Hydrothermal Field, Galapagos Spreading Center. Results from Glomar Challenger piston coring: *J. Geoph. Res.* **88,** 1049–1056.

Buatier, M., Clauer, N., Honnorez, J., and O'Neil, J. M. (1988) A genetic model for hydrothermal Fe-rich clay minerals from Galapagos Spreading Center mounds: XRD, HRTEM, STEM, and isotopic data. GSA meeting, Abstract with programs, Denver, 1988, 72A199.

Ehret, G., Crovisier, J. L., and Eberhart, J. P. (1986) A new method studying leached glasses: Analytical electron microscopy on ultramicrotomic thin sections: *J. Non-Cryst. Solids* **86,** 72–79.

Foster, M. (1960) Interpretation of the composition of trioctahedral micas: *U.S. Geol. Surv. Prof. Pap.* **354-B,** 11–50.

Foster, M. (1969) Studies of celadonite and glauconite: *U.S. Geol. Surv. Prof. Paper* **614-F,** 1–17.

Hendricks, S. B., and Teller, E. (1942) X-ray interference in partially ordered layer lattices: *J. Chem. Phys.* **10,** 147–167.

Hoffert, M., Person, A., Courtois, C., Karpoff, A. M., and Trauth, D. (1980) Sedimentology, mineralogy and geochemistry of hydrothermal deposits from holes 424, 424A, 424B, and 424C (Galapagos Spreading Center): in *Init. Repts. Deep Sea Drilling Project,* **54,** B. R. Rosendahl, R. Hekinian, *et al.*, eds., U.S. Govt. Printing Office, Washington, D.C., 339–376.

Holtzapffel, T., Bonnot-Courtois, C., Chamley, H., and Clauer, N. (1985) Héritage et diagenèse des smectites du domaine sédimentaire nord-Atlantique (Crétacé, Paléocène): *Bull. Soc. Géol. France* **1,** 25–33.

Honnorez, J., Karpoff, A. M., and Trauth Badaut, D. (1983) Sedimentology, mineralogy and geochemistry of green clay samples from the Galapagos hydrothermal mounds, holes 506, 506C, and 507D Deep Sea Drilling Project leg 70: in *Init. Repts. Deep Sea Drilling Project,* **70,** J. Honnorez, R. P. Von Herzen, *et al.*, eds., U.S. Govt. Printing Office, Washington, D.C., 221–224.

Honnorez, J., Von Herzen, R. P., Barret, T. J., Becker, K., Bender, M. L., Bender, P. E., Borella, P. E., Hubberten, H. W., Jones, S. C., Karato, S. I., Laverne, C., Levi, S., Migdisov, A. A., Moorby, S. A., and Schrader, E. L. (1981) Hydrothermal mounds and young ocean crust of the Galapagos: Preliminary Deep Sea Drilling results, leg 70: *Geol. Soc. Amer. Bull.* **92,** 457–472.

Hower, J. (1961) Some factors concerning the nature and origin of glauconite. *Amer. Mineral.* **46,** 313–334.

Inoue, A., Koyama, N., Kitagawa, R., and Watanabe, T. (1987) Chemical and morphological evidence for the conversion of smectite to illite: *Clays & Clay Minerals* **35,** 111–120.

Klitgort, K. D. and Mudie, J. D. (1974) The Galapagos Spreading Center: A near bottom geophysical survey: *Geophys. J. Roy. Astron. Soc.* **38,** 563–586.

Koster, H. M. (1982) The crystal structure of 2:1 layer silicates: in *Proc. 7th Int. Clay Conf., Bologna, Pavia, 1981,* H. van Olphen and F. Veniale, eds., Elsevier, Amsterdam, 41–71.

Kurnosov, V. B., Chudaev, O. V., and Shevchenko, A. Y. (1983) Mineralogy and geochemistry of sediments from Galapagos hydrothermal mounds leg 70, Deep Sea Drilling Project: in *Init. Repts. Deep Sea Drilling Project,* **70,** J. Honnorez, R. P. Von Herzen, *et al.*, eds., U.S. Govt. Printing Office, Washington, D.C., 225–229.

Lalou, C., Brichet, E., Jehanno, C., and Perez-Leclaire, H. (1983) Hydrothermal manganese deposits from Galapagos mounds, D.S.D.P. leg 70, hole 509B and Alvin 3 dives 729 and 721: *Earth Planet Sci. Lett.* **63,** 63–75.

Lee, J. H., Ahn, J. H., and Peacor, D. R. (1985) Textures in layered silicates: Progressive changes through diagenesis and low temperature metamorphism: *J. Sed. Petrol.* **55,** 532–540.

Mossman, J. R. (1987) Conditions physico-chimiques d'évolution de réservoirs gréseux. Approche pétrologique, minéralogique et isotopique. Application aux grès rhétiens du bassin de Paris: Thèse de l'Université Louis Pasteur de Strasbourg, Strasbourg, France, 124 pp.

Paquet, H., Duplay, J., Valleron-Blanc, M. M., and Millot, G. (1987) Octahedral compositions of individual particles in smectite-palygorskite and smectite-sepiolite assemblages: in *Proc. Int. Clay Conf., Denver, 1985,* L. G. Schultz, H. van Olphen, and F. A. Mumpton, eds., The Clay Mineral Society, Bloomington, Indiana, 73–77.

Rinckenbach, T. (1988) Diagénèse minérale des sédiments pétrolifères du delta fossile de la Mahakam (Indonésie). Evolution minéralogique et isotopique des composants argileux et histoire thermique: Thèse de l'Université Louis Pasteur de Strasbourg, Strasbourg, France, 209 pp.

Samuel, J., Rouault, R., and Besnus, Y. (1985) Analyse multiélémentaire standardisée des matériaux géologiques en spectrométrie d'émission par plasma à couplage inductif: *Analusis* **13,** 312–317.

Tessier, D. (1984) Hydration, gonflement et structuration des matériaux argileux au cours de dessication et de réhumectation: Thesis Paris INRA Versailles, Versailles, France, 361 pp.

Thompson, G. R. and Hower, J. (1975) The mineralogy of glauconite: *Clays & Clay Minerals,* **23,** 289–300.

Tixier, R. (1978) Microanalyse sur échantillons minces: in *Microanalyse et Microscope à Balayage. Les éditions de physique,* S. Maurice, L. Meny, and R. Tixier, eds., Orsay, France, 433–448.

Varentsov, I. M., Sakharov, B. A., Drits, V. A. Tsipursky, S. I., Choporov, D. Y., and Aleksandrova, V. A. (1983) Hydrothermal deposits of the Galapagos rift zone, leg 70. Mineralogy and geochemistry of major component: in *Init. Repts. Deep Sea Drilling Project,* **70,** J. Honnorez, R. P. Von Herzen, *et al.*, eds., U.S. Govt. Printing Office, Washington, D.C., 235–268.

Weaver, C. E. and Pollard, L. D. (1973) *The Chemistry of Clay Minerals:* Elesvier, Amsterdam, 213 pp.

Whitney, G. and Northrop, H. R. (1988) Experimental investigation of the smectite to illite reaction: Dual reaction mechanisms and oxygen isotope systematics: *Amer. Mineral.* **73,** 77–90.

Williams, D. L., Von Herzen, R. P., Sclate, J. G., and Anderson, R. N. (1974) The Galapagos Spreading Center: Lithospheric cooling and hydrothermal circulation: *Geophys. J. Roy Astron. Soc.* **38,** 587–608.

Yau, Y. C., Peacor, D. R., and McDowell, S. D. (1987) Smectite-to-illite reactions in Salton Sea shales: A transmission and analytical electron microscopy study: *Sed. Petrol.* **57,** 335–342.

(Received 30 July 1988; accepted 7 February 1989; Ms. 1811)